Low Dimensional Modeling of Zero-Net Mass-Flux Actuators

Quentin Gallas* and Ryan Holman*
University of Florida, Gainesville, Fl, 32608

Reni Raju* and Rajat Mittal†
The George Washington University, Washington DC, 20052

and

Mark Sheplak† and Louis Cattafesta‡
University of Florida, Gainesville, Fl, 32611-6250

The flow field generated by a zero-net mass-flux (ZNMF) actuator is investigated via both numerical simulations and experiments to augment the current understanding of the flow physics of the orifice. The results aid in improving the accuracy of low dimensional lumped element ZNMF models suitable for design. Dimensional analysis yields a number of key parameters that govern the characteristics of this flow. Among them for a sharp rectangular slot or circular orifice are the Reynolds number, the dimensionless stroke length, and the orifice height-to-diameter ratio. Variation of these parameters shows that the flow field differs appreciably from the exact linear solution of pipe flow driven by an oscillatory pressure gradient. In particular, depending on the stroke length and the orifice geometry, the pressure drop in the orifice may be dominated by nonlinear "minor" losses due to entrance/exit effects, or linear "major" losses associated with the presence of a nominally fully-developed region in the central region of the orifice/slot.

I. Introduction

ZERO-net mass-flux (ZNMF) actuators, also known as synthetic jets, have emerged as versatile actuators in various applications (e.g., thrust vectoring of jets,[1] active control of separation[2,3,4,5] and turbulence in boundary layers[5,7]). ZNMF actuators exhausting into a quiescent medium have been studied both experimentally[8,9,10] and numerically,[11,12] while other studies have focused on the interaction with an external boundary layer.[13,14,15,16] However, numerous unresolved issues remain concerning the fundamental governing physics of these devices, effectively hindering their modeling, design and optimization. For example, the unsteady flow in the orifice or slot plays a large role in determining the actuator performance. While numerous parametric studies have examined various orifice geometry and flow conditions, a clear understanding of the loss mechanisms is still lacking. Detailed numerical simulations (and companion experiments) can be used to elucidate the underlying physics but are not practical as a design tool. Instead, accurate low dimensional models are required to facilitate the effective design of ZNMF actuators for specific applications.

Fig.1 shows a simple schematic of a typical ZNMF actuator. Fluctuating flow in the slot is induced by the oscillation of the driver mounted in a cavity of volume $\forall$ using, for example, a piezoelectric diaphragm or an electromagnetic piston, etc. The diaphragm deflection is characterized by its volume displacement $\Delta\forall$ as a function of the angular frequency ω. The orifice geometry is described by its height h and diameter d for a sharp-edged axisymmetric orifice and similarly for a two-dimensional slot.

* Graduate Student, Department of Mechanical and Aerospace Engineering, Student Member AIAA.
† Associate Professor, Department of Mechanical and Aerospace Engineering, Senior Member AIAA.
‡ Associate Professor, Department of Mechanical and Aerospace Engineering, Associate Fellow AIAA.

With regards to the nature of the unsteady flow in the orifice and the associated losses, it is instructive to first consider the simpler case of *steady* flow through a pipe. In this case, losses arise due to different mechanisms. In any undergraduate fluid mechanics textbook, these losses are characterized as "major" losses in the fully developed flow region and "minor" losses associated with entrance and exit effects, etc. For laminar flow, the pressure drop Δp in the fully-developed region is *linearly* proportional to the volume flow rate Q or average spatial velocity u_{avg}, while the *nonlinear* minor pressure losses are proportional to the dynamic pressure $0.5\rho u_{avg}^2$. Similarly, for the case of *unsteady*, laminar, fully-developed, flow driven by an oscillatory pressure gradient, the complex flow impedance, $\Delta p'/Q'$, can be determined analytically and decomposed into linear resistance and reactive components.[17] Unfortunately, no such solution is available for the nonlinear, and perhaps dominant, losses associated with entrance and exit effects. The lumped element model of McCormick[18] uses the limiting steady flow solution for $\Delta p'/Q'$, while that of Gallas et al.[19] uses the frequency-dependent analytical solution for the linear resistance. However, both models suffer from an overly simplistic empirical equation for the nonlinear resistance component.

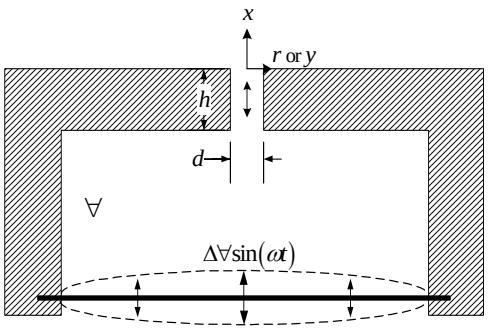

Figure 1. Schematic of a typical ZNMF actuator.

An alternative approach to characterize or "calibrate" an oscillatory fluidic actuator uses the empirical observation that the cavity pressure fluctuation $\Delta p'$ is linearly proportional to the centerline exit velocity fluctuation u' at low forcing levels and $\propto u'^2$ (i.e., nonlinear) at sufficiently high forcing levels.[20,21] However, the relative importance and scaling of the linear and nonlinear components versus the governing dimensionless parameters is unknown and remains a critical obstacle for designers of ZNMF actuators.

This paper presents the progress in an ongoing collaborative effort focused on the development of low-dimensional models for ZNMF actuators. While the ultimate goal is to develop models suitable for use in boundary layer flow control in which the ZNMF actuator interacts with a grazing flow, the current paper focuses on experimental and computational efforts to first understand and model the oscillatory orifice flow in the simpler case without a grazing flow. As such, similar to the recent work by Smith & Swift who experimentally studied the losses in an oscillatory flow through a *rounded* slot,[22] this paper focuses on the more commonly employed *sharp-edged* orifice or slot of a ZNMF actuator. In particular, experimental data and numerical simulations are used to explore the flow behavior and develop components for a low-order lumped element model of a ZNMF actuator. The effects of various governing dimensionless parameters are examined. The paper is organized as follows. Following a dimensional analysis, the details of the experimental and computational methods are presented. The remainder of the paper focuses on analysis of the resulting data to elucidate the flow physics and to develop a model for nonlinear resistance. Finally, preliminary conclusions are offered, and future work is discussed.

II. Nondimensional Parameters

The geometry of the flow under consideration is shown in Fig. 1. The governing dimensionless parameters for a ZNMF actuator include a Reynolds number and either a normalized stroke length or a Strouhal number. Various velocity scales are employed in the literature, but the present work employs the spatial-averaged, time-averaged exit velocity during the expulsion portion of the cycle:

$$\bar{U}_j = \frac{2}{T}\frac{1}{A_n}\int_{A_n}\int_0^{T/2} u(t,y)\,dt dA = \frac{2}{T}\int_0^{T/2} u_{avg}(t)\,dt\,, \tag{1}$$

where $T = 1/f = 2\pi/\omega$ is the period of the cycle, A_n is the orifice area, and $u_{avg}(t)$ is defined as the spatial-averaged, axial component of the velocity at the exit plane. The stroke length L_0, which is a measure of the distance that a fluid particle travels during the expulsion part of the cycle, is thus defined as

$$L_0 = \int_0^{T/2} u_{avg}(t)\,dt = \bar{U}_j \frac{T}{2}\,. \tag{2}$$

Note the equivalence between the different dimensionless parameters. The Strouhal number is defined as $St = \omega d / \bar{U}_j$; thus the following relationship exists between the Strouhal number, Stokes number $S = \sqrt{\omega d^2 / \nu}$, Reynolds number $\mathrm{Re}_j = \bar{U}_j d / \nu$, and the dimensionless stroke length L_0/d:

$$\frac{1}{St} = \frac{\mathrm{Re}_j}{S^2} = \frac{L_0/d}{\pi}. \tag{3}$$

A dimensional analysis of a ZNMF actuator with a sharp-edged rectangular 2-D slot or orifice using a generic driver and exhausting in a quiescent medium reveals the following functional form:

$$\left(St, \mathrm{Re}_j\right) = f\left(\frac{\omega}{\omega_H}, \frac{h}{d}, \frac{\omega}{\omega_d}, \frac{\Delta\forall}{d^3}, kd, S\right). \tag{4}$$

The two parameters on the LHS are both primarily dependent on $\bar{U}_j$. The terms on the RHS are explained as follows: The ratio of the driving frequency to the Helmholtz frequency ω/ω_H is a measure of the compressibility of the flow inside the cavity. The flow in the cavity is essentially incompressible provided that $\omega/\omega_H \ll 1$. Hence, incompressible CFD models are only relevant for this case. Note that $\omega_H = c_0\sqrt{A_n/h'\forall}$ is based on the isentropic sound speed c_0, the neck area A_n, the effective height of the neck h', and cavity volume $\forall$. Hence, the condition $\omega/\omega_H \ll 1$ is satisfied for a sufficiently small cavity volume. Next, ω/ω_d is the ratio of the drive frequency to the natural frequency of the driver, and $\Delta\forall/d^3$ is the dimensionless displacement of the driver. The parameter $kd = 2\pi d/\lambda$ is related to the ratio of the orifice diameter to the acoustic wavelength. The Stokes number S can be interpreted as the ratio of the orifice diameter to the unsteady boundary layer thickness in the orifice $\sqrt{\nu/\omega}$. Eq. (4) forms the basis for the selection of our test matrix, which for the purposes of studying the oscillatory flow in the orifice, consists of h/d, Re_j, and S (or, by virtue of Eq. (3), L_0/d or St).

III. Experimental Setup

Fig. 2 shows a schematic of the experimental setup. A piezoelectric diaphragm is actuated using an Agilent 33120A function generator with an amplifier. Cavity pressure measurements are obtained using a flush-mounted Brüel and Kjær (B&K) 1/8″ diameter condenser type microphone (Model 4138) powered by a B&K 2670 pre-amplifier and a B&K 2804 power supply. In addition, the centerline deflection of the diaphragm is measured using a laser displacement sensor (Micro-Epsilon Model ILD2000-10). Both signals are acquired phase-locked to the drive signal and sampled simultaneously with a dynamic signal analyzer (National Instruments Model 4552).

Velocity measurements of the flowfield emanating from the ZNMF orifice are acquired using Laser Doppler Anemometry (LDA), the details of which are listed in Table 1. The synthetic jet actuator is mounted to a three-axis traverse with sub-micron spatial resolution. The 488 and 514.5 nm lines of an argon-ion laser are used to obtain coincident, two-component velocity measurements using a Dantec FiberFlow system. As shown in Fig. 3, a novel three-beam optical combiner configuration is used to facilitate velocity

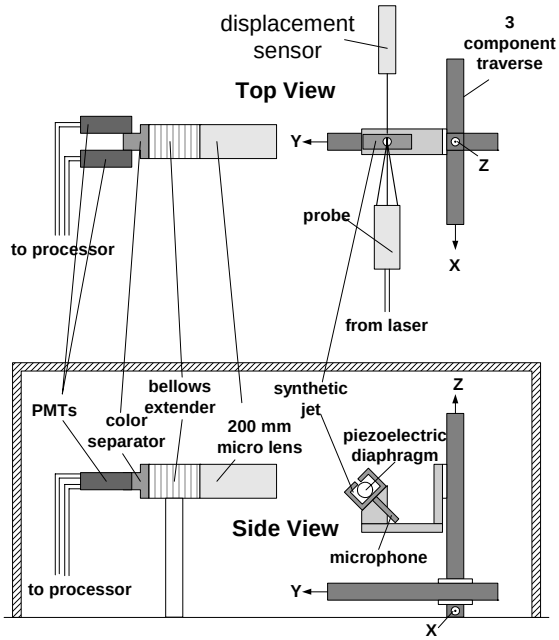

Figure 2. Schematic of the experimental setup for off-axis, two-component LDA measurements.

Table 2. LDA measurement details.

Property:	LDA 1	LDA 2
Wavelength (nm)	514.5	488
Focal length (mm)	120	120
Beam diameter (mm)	1.35	1.35
Beam spacing (mm)	26.87	26.87
Number of fringes	25	25
Fringe spacing (μm)	2.3121	2.1929
Beam half-angle (deg)	6.39	6.39
Probe volume – *dx* (mm)	0.0586	0.0556
Probe volume – *dy* (mm)	0.0582	0.0552
Probe volume – *dz* (mm)	0.5233	0.4963

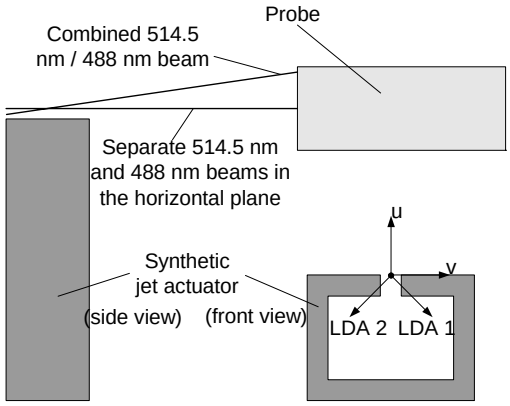

Figure 3. LDA 3-beam optical configuration.

Table 1. Synthetic jet actuator details.

Property:	Value:
Cavity volume $\forall$ (m^3)	7.11×10^{-6}
Orifice diameter *d* (mm)	2.00
Orifice thickness *h* (mm)	1.65

measurements at the exit plane of the synthetic jet actuator (see Table 2). A direction cosine transformation is then applied to the acquired velocity components LDA 1 and LDA 2 to extract the axial and radial velocity components.

A 200 mm micro lens and bellows extender collects lights at 90º off-axis in order to improve the spatial resolution. Scattered light from the probe volume is focused and passed through a 100 μm diameter pinhole aperture. The resulting field of view was imaged using a micro-ruler and found to be approximately 10 μm, indicating that the effective length of the probe volume *dz* has been reduced by over an order of magnitude from that listed in Table 1. After the pinhole, a color separator splits the 514.5 nm and 488 nm wavelengths and transmits the light to two separate photomultiplier tubes (PMTs) for subsequent FFT analysis.

Phase-locked velocity measurements are acquired at the centerline of the jet exit with a resolution of 10º and approximately 200 velocity values are acquired at each phase angle. In addition, the synthetic jet device is traversed to acquire phase-locked velocity profiles across the surface of the orifice with a spatial resolution of 0.1 mm for select cases.

Once the velocity profiles at the surface of the orifice are acquired, the phase-locked profiles are spatially integrated to determine the periodic volume flow rate. The velocity profiles are phase-locked to the other measured signals via the TTL trigger signal available on the function generator. In the data presented in this paper, zero phase is defined as the point at which the volume flow rate is zero with positive slope.

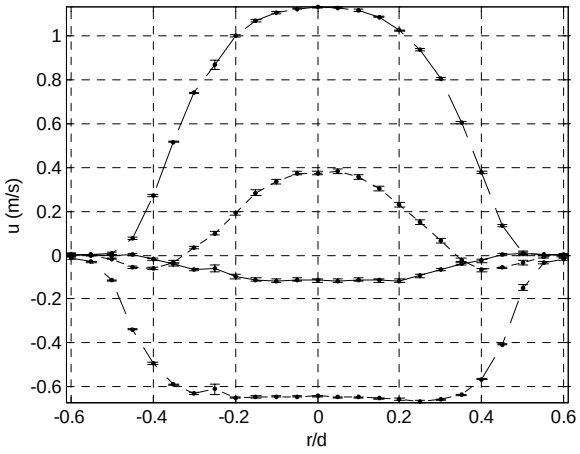

Figure 4. Phase-locked axial velocity profiles at x/d=0.07, S=8, Re_j =45.5.

Fig. 4 illustrates a set of typical phase-locked axial velocity profiles during four different phases separated by 90º in the cycle, corresponding to maximum expulsion, maximum ingestion, and the two phases half way between. The error bars represent an estimate of the 95% confidence interval for each velocity measurement and are obtained using a perturbation technique[23] that yields the same nominal values of uncertainty as a standard Monte Carlo technique but with significantly less computational time. This method is employed to estimate the uncertainty in the volume flow rate. The circular orifice was observed under a microscope and found to have a diameter $d = 2 \pm 0.06$ mm. The 95% confidence intervals estimates of $\bar{Q}_j$ and d, in turn, are used to estimate the uncertainty in the Reynolds number, which is in the range of 2-10%.

The locus of the positive values of the volume flow rate are integrated to give the average volume flow rate during the expulsion part of the cycle, $\bar{Q}_j$, which is related to the average velocity by $\bar{Q}_j = \bar{U}_j \pi d^2 / 4$. Thus, the Reynolds number is given by

$$\mathrm{Re}_{\bar{U}_j} = \frac{4\bar{Q}_j}{\pi \nu d}. \tag{5}$$

IV. Numerical Methodology

An in-house, cell-centered based Cartesian grid solver is used for simulating the flow generated by a ZNMF actuator. The incompressible Navier-Stokes equations are used since $\omega/\omega_H \ll 1$ and are non-dimensionalized with appropriate length and velocity scales and discretized using a cell-centered, collocated (non-staggered) arrangement of the primitive variables velocities $\vec{u}$ and pressure p. In addition to the cell-center velocities ($\vec{u}$), the face-center velocities $\vec{U}$ are computed. Similar to a fully staggered arrangement, only the component normal to the cell-face is calculated and stored. The face-center velocity is used for computing the volume flux from each cell. The advantage of separately computing the face-center velocities was initially proposed by Zang et al.[24] and discussed in the context of the current method in Ye et al.[25] A second-order Adams-Bashforth scheme is employed for the convective terms, while the diffusion terms are discretized using an implicit Crank-Nicolson scheme which eliminates the viscous stability constraint. The pressure Poisson equation is solved with a Krylov-based approach.

A multi-dimensional ghost-cell methodology is used to incorporate the effect of the immersed boundary on the flow.[26] The schematic in Fig. 5 (a) shows a solid body with a curved boundary moving through a fluid and the categorization of the nodes for the purpose of implementing the ghost cell methodology. For moving boundaries, the general framework can be considered as Eulerian-Lagrangian, wherein the immersed boundaries are explicitly tracked as surfaces in a Lagrangian mode, while the flow computations are performed on a fixed Eulerian mesh. Hence, we identify cells that are just inside the immersed boundaries as "ghost cells." The discrete equations for these cells are then formulated as to satisfy the imposed boundary condition on the nearby flow boundary to second-order accuracy. These equations are then solved in a fully coupled manner with the governing flow equations of the regular fluid cells. Care has been taken to ensure that the equations for the ghost cells satisfy local and global mass conservation constraints as well as pressure-velocity compatibility relations. The solver has been designed to take geometrical input from conventional CAD programs. The code has been well validated by comparisons against established experimental and computational data.[27] The solver is currently being used to carry out parametric studies of synthetic jets in both quiescent and grazing flow fields.[14] The typical 2-D setup for a rectangular synthetic jet in quiescent flow field is as shown in Fig. 5 (b). For the numerical simulations described here, a pulsatile boundary condition is provided at the bottom of the cavity.

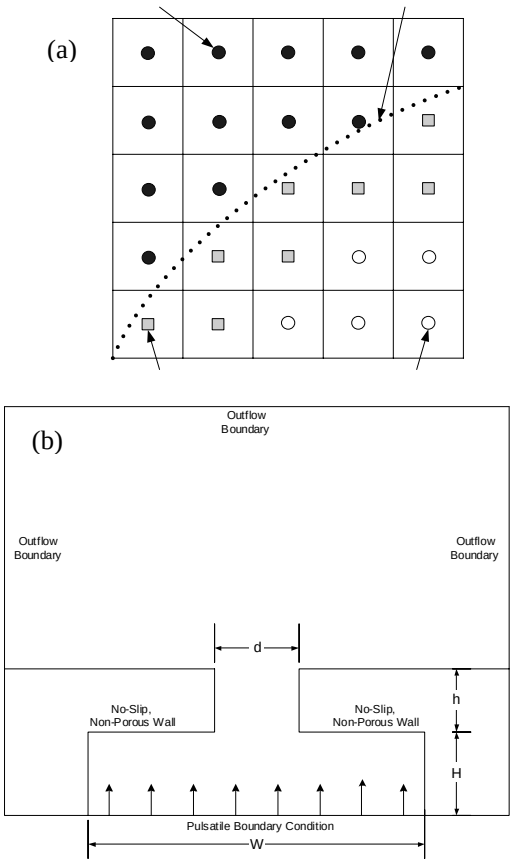

Figure 5. (a) Schematic of the sharp-interface method on a fixed Cartesian mesh and (b) synthetic jet computational boundary conditions.

V. Lumped Element Modeling

The low dimensional modeling approach adopted is based on lumped element modeling (LEM).[18,19] In LEM, the individual components of a synthetic jet are modeled as elements of an equivalent electrical circuit using conjugate power variables (i.e., power = generalized "flow" × generalized "effort" variables). Fig. 6 shows an equivalent circuit representation of a piezoelectric-driven synthetic jet actuator, where the lumped parameters represent generalized energy storage elements (i.e., capacitors and inductors) and dissipative elements (i.e., resistors). Model parameter estimation techniques, assumptions, and limitations are discussed in Gallas et al.[19] The frequency response function of the circuit is derived to obtain an expression for Q_j/V_{ac}, the jet volume flow rate during the expulsion part of the cycle per applied voltage. LEM provides a compact nonlinear analytical model and valuable physical insight into the dependence of the device behavior on geometry and material properties. However, the primary difficulty with this method is the lack of sufficient physics in the orifice impedance models, embodied as linear and nonlinear resistors and masses, as shown in Fig. 6.

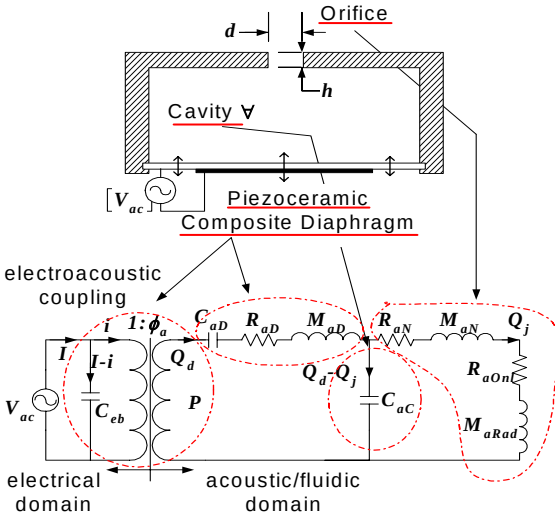

Figure 6. Equivalent circuit model of a piezoelectric-driven synthetic jet actuator.

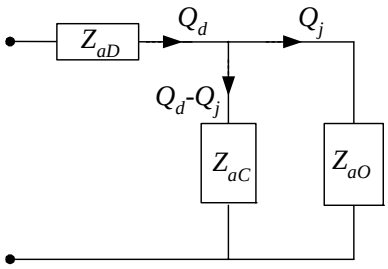

Figure 7. Volume velocity divider circuit, valid for a generic ZNMF actuator.

With slight modifications, the model is applicable to any type of ZNMF actuator (electromagnetic, etc.) and for two-dimensional slots and axisymmetric orifices. Fig. 7 shows a current divider circuit that is applicable to a generic driver provided that the motion (i.e., the volume velocity Q_d) of the driver is known.

The sinusoidal volume velocity of the driver is $Q_d = j\omega\Delta\forall\sin(\omega t)$, where $\Delta\forall$ is the net volume displaced by the driver motion. Q_d is split into two paths, and the flow takes the path of least impedance. Essentially, the driver can compress or expand the fluid in the cavity $(Q_d - Q_j)$ and expel or ingest fluid through the orifice (Q_j). The governing equation is given by

$$Q_j = \frac{Q_d Z_{aC}}{Z_{aO} + Z_{aC}}, \tag{6}$$

where $Z_{aC} = 1/j\omega C_{aC}$ is the acoustic impedance of the cavity, and the acoustic impedance of the orifice is given by $Z_{aO} = R_{aN} + R_{aOnl} + j\omega(M_{aN} + M_{aRad})$. If desired, elementary circuit laws can be used to derive a nonlinear 2nd-order ODE that describes the flow in the orifice.

The nonlinear resistance R_{aOnl} is associated with entrance and exit losses and is usually modeled as a generalized Bernoulli flow meter like a minor "dump" loss[18]

$$R_{aOnl} = \Delta p/Q_j = 0.5K_D\rho Q_j/A_n^2, \tag{7}$$

where the dimensionless loss coefficient $K_D = \Delta p \Big/ \left(0.5\rho u_{avg}^2\right)$ was assumed to be unity in ref. 18 and 19. In the more general case, K_D is a function of geometry, Reynolds number, and in the case of oscillatory flow, Stokes number (or dimensionless stroke length or Strouhal number). Furthermore, if the geometry is not symmetric, then the loss coefficient may be different for the inlet and exit portions of the cycle. Hence, a detailed analysis on the loss coefficient for various orifice shapes, such as that of Smith and Swift[22] for a rounded edge, should yield a more accurate expression in terms of modeling the associated nonlinear resistance. The results presented below summarize efforts at assessing (1) the accuracy of Stokes oscillating pressure gradient solution to estimate the linear impedance and (2) the variation of K_D as a function of Reynolds number and Stokes number.

VI. Results

Table 3 shows the test matrix employed to conduct the experimental and numerical study of the oscillatory flow through a ZNMF actuator orifice by varying h/d, Re_j, and S. (In addition, also listed for convenience are h/L_0 and ω/ω_H, as well as whether a jet is formed or not from the criterion based on the ratio Re_j/S^2 [28, 29]). Cases 1-4 are experiments, while Cases 5-7 are computations. It should be noted that 10 additional experimental cases similar to cases 1 and 2 have been studied with h/d =0.82 and S =8 by varying Re_j from 9 to 94. Similarly, 16 additional experimental cases similar to cases 3 and

Table 3. Test Matrix.

Case	Jet formed	h/d	Re_j	S	h/L_0	ω/ω_H
1 (exp.)	yes	0.82	45	8	0.37	0.05
2 (exp.)	yes	0.82	94	8	0.18	0.05
3 (exp.)	no	0.82	185	36	1.82	0.93
4 (exp.)	yes	0.82	1136	36	0.29	0.93
5 (num.)	no	1	262	25	0.76	0.13
6 (num.)	no	2	262	25	1.52	0.09
7 (num.)	yes	0.68	262	10	0.08	0.18

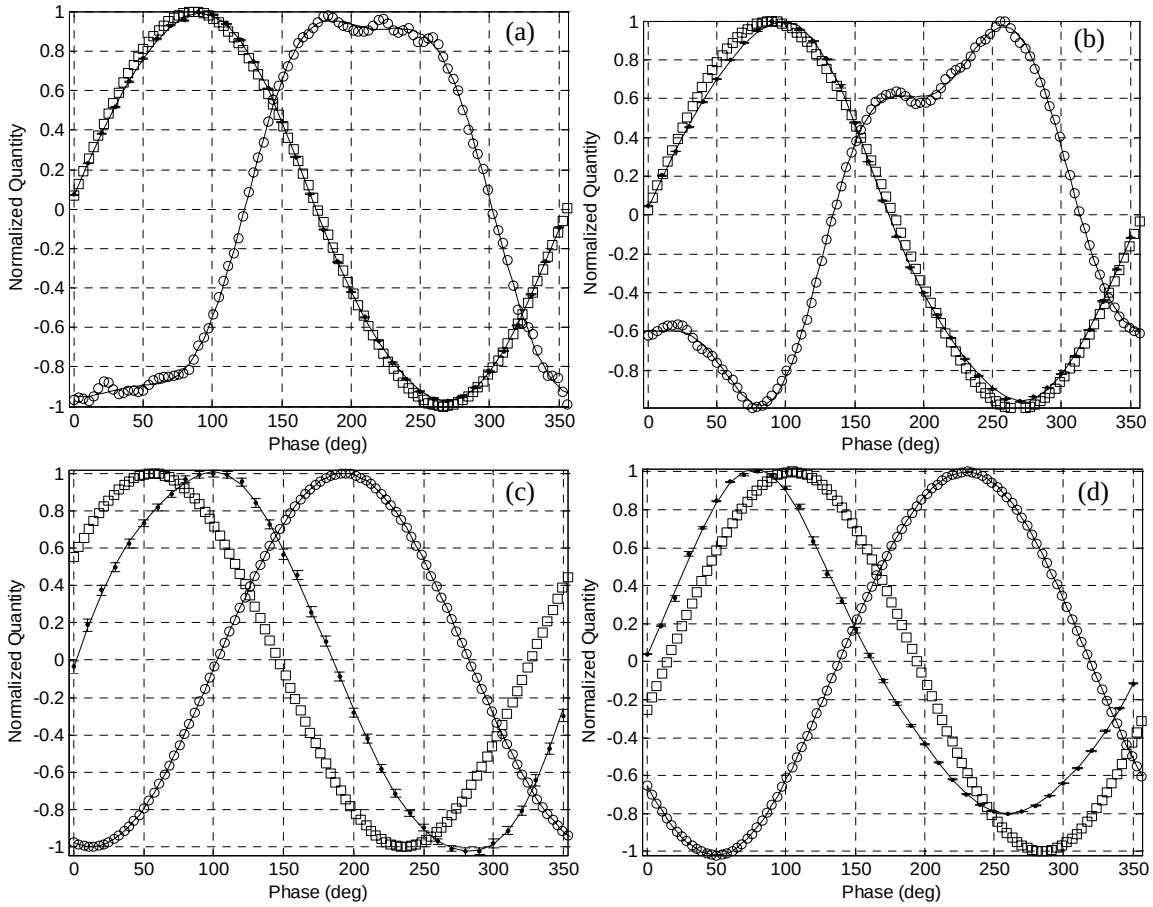

Figure 8. Normalized quantities vs. phase for (a) Case 1, (b) Case 2, (c) Case 3, and (d) Case 4: (•) volume flow rate, (○) cavity pressure, (□) centerline driver velocity.

4 have been studied with h/d =0.82 and S =36 by varying Re_j from 185 to 1875. However, only the phase locked centerline velocity was acquired for these cases, while for the first four cases listed in Table 3, velocity profiles were acquired across the orifice exit.

Volume flow rate, cavity pressure, and centerline driver velocity are shown phase locked in Fig. 8 for Cases 1 through 4, where zero phase corresponds to zero volume flow rate with a positive slope. The measured driver displacement has been differentiated to obtain the driver velocity. The interesting point to note is that, for Cases 1 and 2 with S =8 and ω/ω_H =0.05, the volume flow rate and centerline driver velocity are nearly in phase, indicating that the flow is incompressible. In contrast, for Cases 3 and 4 with S =36 and ω/ω_H =0.93, the orifice volume flow rate is not in phase with the driver velocity, ostensibly due to compressibility effects in the cavity.

The cavity pressure fluctuation deviates from a sinusoid for Cases 1 and 2, indicating significant nonlinearity despite the low Re_j. In contrast, in Cases 3 and 4, the pressure oscillations are nearly perfect sinusoids, indicating linear oscillations despite the significantly larger Re_j. A possible explanation for the observed behavior is discussed further below.

Although not shown here, a spectrum analysis has been performed on the pressure traces in order to characterize the dominant features of the distorted time signals. It was found that only subharmonics were present, with the total power being dominated by the one due to the fundamental frequency. Furthermore, in order to ascertain the resistance and reactance terms in the orifice, both the amplitude and relative phase between the pressure fluctuations and volume flow rate at the drive frequency are required. Fig. 8 also plots the waveforms for both volume flow rate and pressure determined from the first three terms of a Fourier decomposition via least squares estimation. Despite the significant deviation from a sinusoidal profile in the pressure fluctuation for Case 2 for example, the Fourier decomposition provides a good representation. The relative phase between the fundamentals of the pressure and volume flow rate can then be extracted at the fundamental frequency.

Utilizing the data acquired from the additional cases as described above, Fig. 9 plots the fluctuating pressure normalized by the dynamic pressure based on the centerline velocity U_{CL} vs. L_0/h, the ratio of the stroke length to the orifice height. Before commenting on these data, note that the stroke length L_0 requires knowledge of the velocity profile. Since the velocity profiles are not available for all cases, $\bar{U}_j$ is estimated by computing the ratio $\bar{U}_j/U_{CL}$ for each Stokes number based

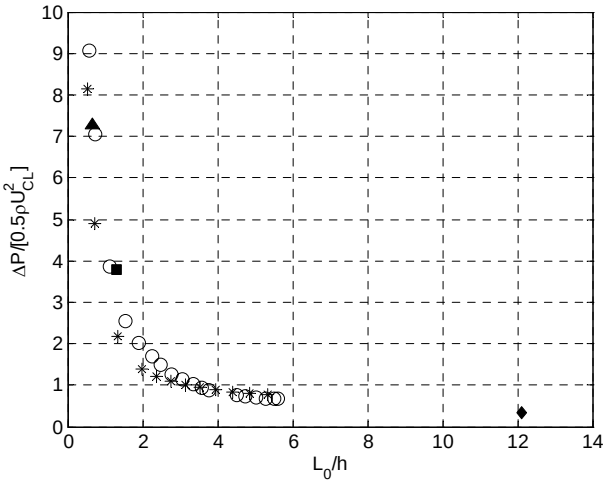

Figure 9. Pressure fluctuation normalized by dynamic pressure based on centerline velocity vs. L_0/h : (*) S=8, 9< Re_j <90; (○) S=36, 190< Re_j <1875; (▲) Case 5; (■) Case 6; (♦) Case 7.

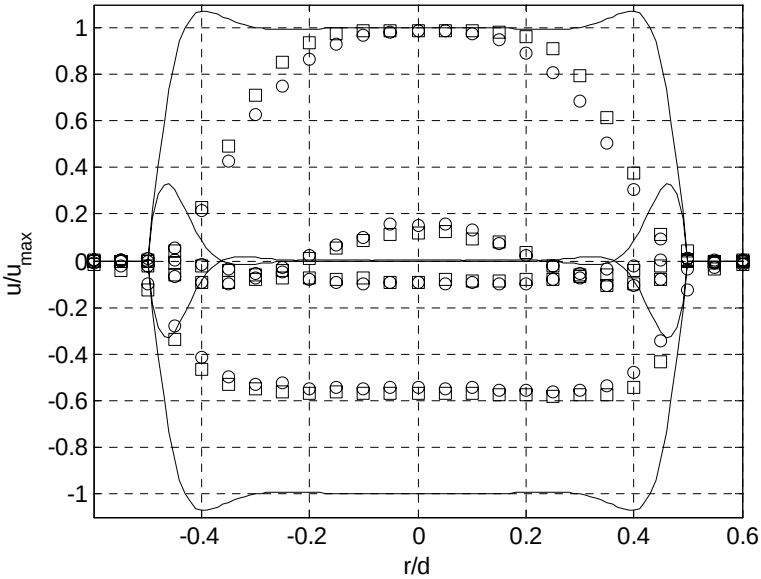

Figure 10. Normalized axial velocity profiles at four phases during a cycle for S=8, (○) Re_j = 45.5 , (□) Re_j = 94 , (–) solution for pipe flow with an oscillating Δp .

on the profiles obtained for Cases 1-4. As shown in Fig. 10, this ratio is approximately constant for a given Stokes number and invariant as the Reynolds number changes. However, the measured exit velocity profile shape *does not* agree with the theoretical profile for oscillatory pipe flow[30] as shown in Fig. 10, especially during the suction stroke.

Returning to Fig. 9, the pressure loss data asymptote to a value of approximately 0.75 as L_0/h increases beyond a value of ~4. This suggests that when the fluid particle excursion or stroke length is much larger than the orifice height h, minor "nonlinear" losses due to entrance and exit effects dominate the flow. However, the magnitude of these losses and the degree of nonlinear distortion is likely to be strongly dependent on Reynolds number. For shorter stroke lengths, as in Case 3 shown in Fig. 8(c), when the particle excursion is smaller than h, the flow presumably approaches a fully-developed state, and major losses which scale with u' dominate the minor losses. Here, "fully developed" means that there exists a region within the orifice away from either exit, where the velocity profile at a given point during the cycle is not a function of axial position x.

The results of the CFD simulations allow us to explore this hypothesis further. Fig. 11 shows the variation of the spanwise vorticity for the three computational cases (5, 6 ,and 7). For Cases 5 & 6, no jet is formed as seen in Fig. 11(a) and (b). The vorticity contours show that vortices formed during the expulsion cycle for these cases are ingested back during the suction cycle, leading to the trapping of vortices inside the orifice and increased losses over and above that predicted by linear theory. In contrast, clear jet formation occurs for Case 7 as shown in Fig. 11(c). These results are consistent with the jet formation criterion proposed by Utturkar[28] and Utturkar et al.[29], which have shown that jets are formed above a critical value of $\mathrm{Re}_j/S^2 > 0.16$ and 1 for a sharp orifice and 2-D slot, respectively. The flow is qualitatively the same for Cases 5 and 6 despite the doubling of h, suggesting that orifice height plays a relatively minor role in determining jet formation.

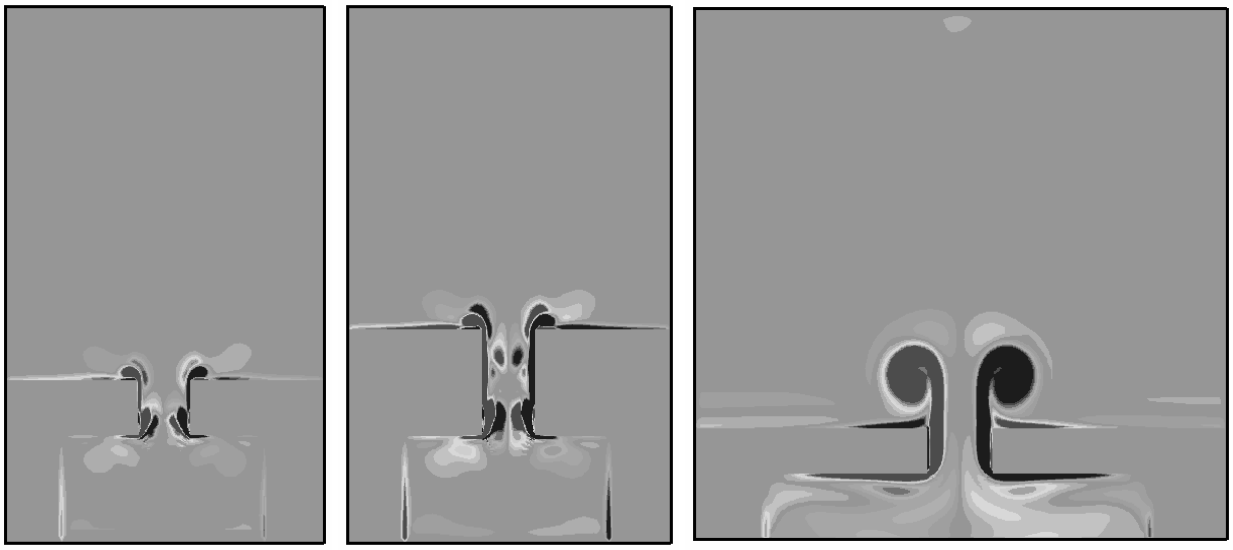

Figure 11. Vorticity contours during the maximum expulsion portion of the cycle for (a) Case 5, (b) Case 6, and (c) Case 7.

Next, temporal variations of the pressure as a function of location along the slot and volume flow rate obtained from the numerical simulations are shown in Fig. 12. A comparison of the pressure traces shows a significant phase shift in the pressure (see probe 1 position) in the jet formation case (Case 7) with the largest stroke length compared to Cases 5 and 6. Furthermore, all of the pressure traces in Case 7 show significant nonlinear distortion, a behavior which is similar to that seen for the low Stokes number Cases 1 and 2 in Fig. 8, both of which correspond to jet formation. The deviation of the pressure signal from a sinusoidal shape is a clear indication that the periodic ejection and ingestion of strong vortices has a major effect on the resistance characteristics of the orifice. However, for the highest Reynolds number (Case 4), the nonlinear losses are reduced in magnitude such that the pressure distortion in Fig. 8(d) is not evident.

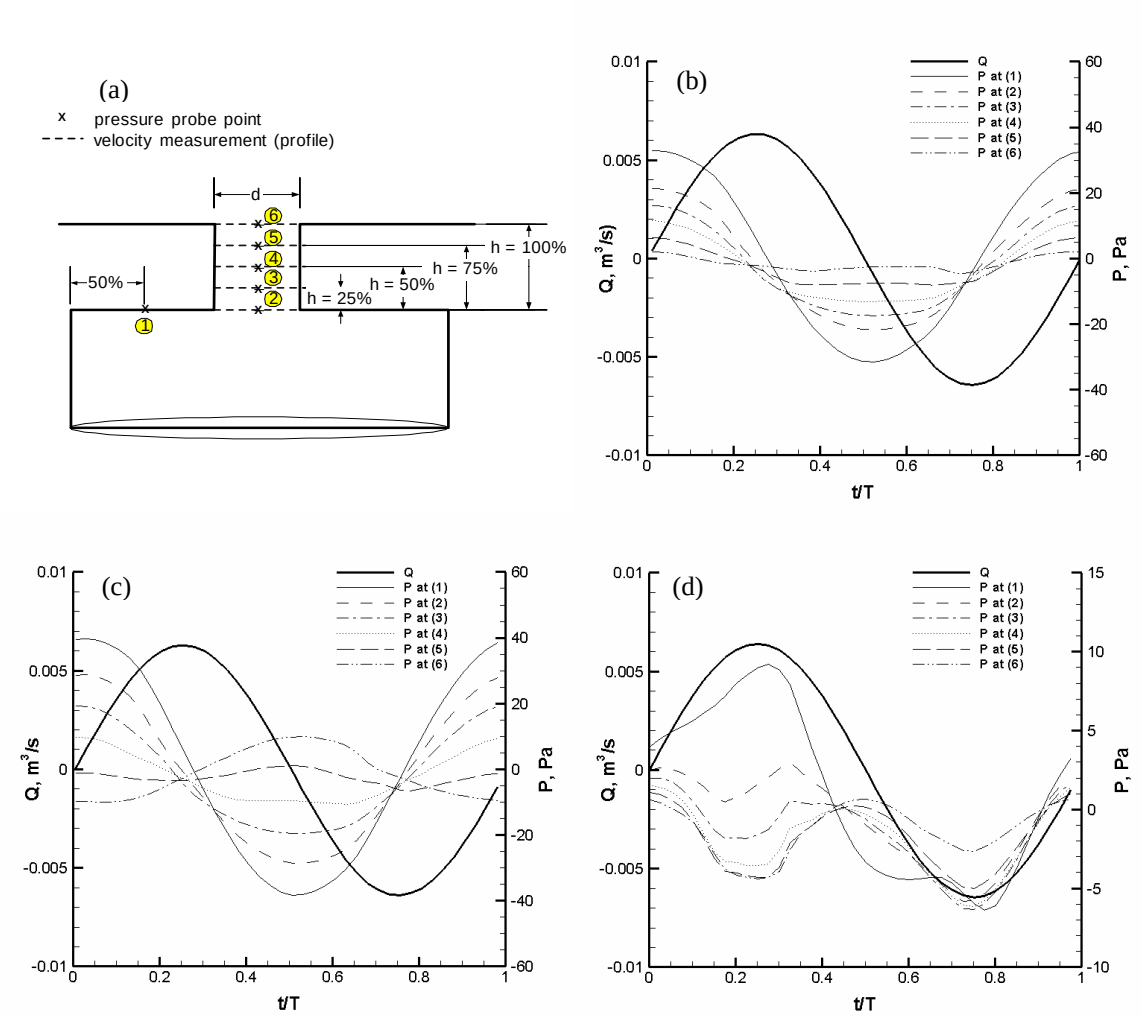

Figure 12. (a) Probe positions in numerical simulations. Volume flow rate/pressure at various locations inside the orifice for (b) Case 5, (c) Case 6 and (d) Case 7 during a cycle. The pressure at probes 2 to 6 are spatially averaged pressure across the orifice.

The CFD data permits the examination of the evolution of the velocity profile inside the slot. Fig. 13 shows the computed velocity profiles at various locations in the orifice corresponding to the maximum expulsion phase. As with the pressure, Cases 5 and 6 are qualitatively similar, and both show that the velocity profile undergoes significant development along the length of the slot. A close examination of flow animations reveals the strong periodic influence of the vorticity as it is expelled and then ingested again. This effect is presumably enhanced by the sharp corners of the slot compared to the rounded edges studied by Smith and Swift.[22] In contrast, the evolution of the velocity profiles for Case 7, in which a jet is formed, is significantly different from the previous two cases. For this case, where the stroke length is much larger than the orifice height, the core flow moves in phase at each location inside the orifice. Furthermore, it appears that the flow approaches a quasi-steady behavior for large L_0/h and is dominated by entrance and exit losses, the magnitude of which are inversely proportional to Reynolds number.

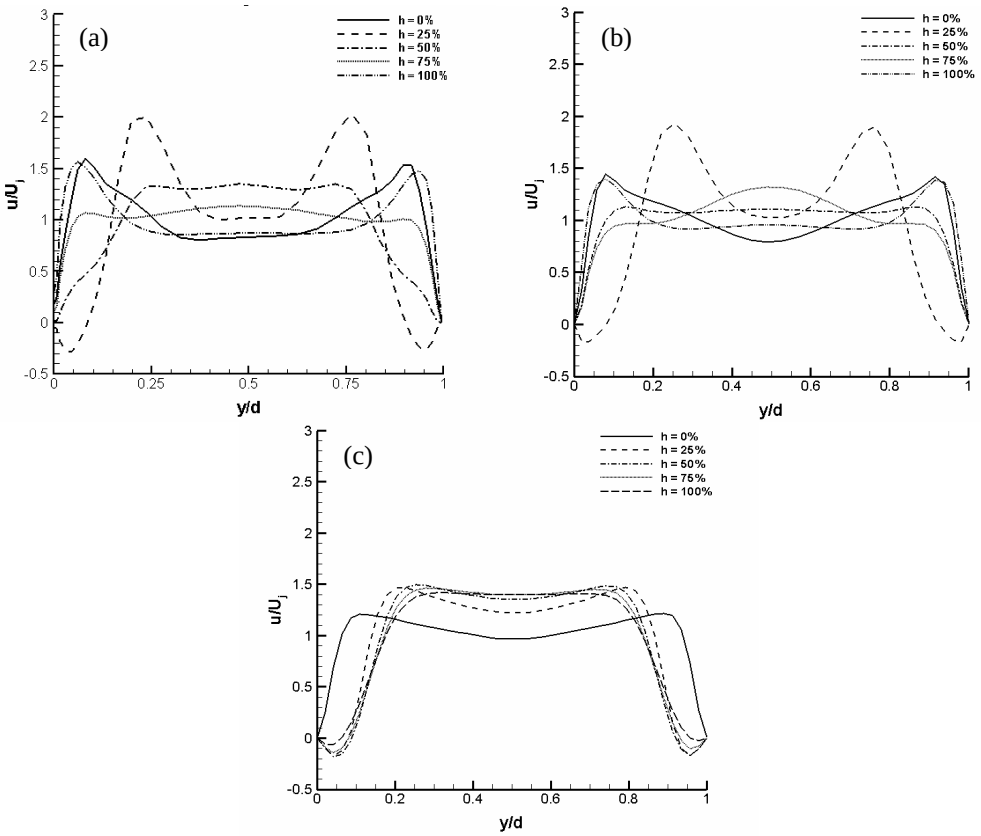

Figure 13 . Velocity profile at different location inside the orifice, during the maximum expulsion portion of the cycle. (a) Case 5, (b) Case 6 and (c) Case 7. The locations are indicated in Figure 12(a).

VII. Conclusions & Future Work

A thorough understanding of the unsteady flow behavior and associated losses in the orifice/slot of zero-net mass-flux devices is critical for the development of accurate low-order models suitable for design. This experimental and computational study has examined ZNMF devices exhausting into a quiescent medium. The geometry is characterized by a sharp-edged, axisymmetric orifice or its 2-D slot counterpart. It has been found that the flow field emanating from the orifice/slot is characterized by both linear and nonlinear losses. Due to the sharp-edged geometry, the linear losses are under predicted by the theoretical linear solution for pipe/channel flow driven by an oscillating pressure gradient. Furthermore, the flow field inside the orifice may vary significantly from the linear solution due to the persistent presence of vorticity in the orifice from previous expulsion/ingestion cycles. Nevertheless, it was found that the pressure drop in the orifice, when normalized by the dynamic pressure based on the amplitude of the flow centerline velocity, collapsed at high dimensionless stoke lengths over a range of Reynolds and Stokes numbers in the experiments and simulations. When the stroke length is large compared to the orifice height, this dimensionless pressure drop is small, O(0.75), presumably because the flow is dominated by nonlinear minor losses associated with entrance effects. However, when the stroke length is small, the pressure drop rises, presumably due to the lower Reynolds numbers and the major losses typical of fully-developed flows.

In future experiments and simulations, additional Stokes numbers and values of h/d will be investigated. It is anticipated that the additional experimental and computational data will permit a physics-based empirical correlation for the nonlinear loss coefficient as a function of Reynolds number and stroke length.

VIII. Acknowledgments

This work was supported by grants from the Air Force Office of Scientific Research, USAF (F49620-03-1-0135 and F49620-01-1-0146).

IX. References

[1] Smith, B. L. and Glezer, A., "Jet Vectoring Using Synthetic Jet Actuators," *JFM*, Vol. 458, pp. 1-34, 2002.

[2] Wygnanski, I., "Boundary Layer and Flow Control by Periodic Addition of Momentum," AIAA 97-2117, 1997.

[3] Crook, A., Sadri, A. M. and Wood, N. J., "The Development and Implementation of Synthetic Jets for the Control of Separated Flow," AIAA 99–3176, 1999.

[4] Holman, R., Gallas, Q., Carroll, B., and Cattafesta, L., "Interaction of Adjacent Synthetic Jets in an Airfoil Separation Control Application," AIAA 2003-3709, 2003.

[5] Seifert, A. and Pack, L. G., "Oscillatory Control of Separation at High Reynolds Numbers," *AIAA J.*, Vol. 37, No. 9, 1999.

[6] Lee, C. Y., and Goldstein, D. B., "DNS of Microjets for Turbulent Boundary Layer Control," AIAA 2001-1013, 2001.

[7] Rathnasingham, R. and Breuer, K. S., "Active Control of Turbulent Boundary Layers," *JFM*, Vol. 495, pp. 209-233, 2003.

[8] Smith, B. L. and Glezer, A., "The Formation and Evolution of Synthetic Jets," *Phys. Fluids*, Vol. 10, No. 9, 1998.

[9] Rathnasingham, R. and Breuer, K. S., "Coupled Fluid–Structural Characteristics of Actuators for Flow Control," *AIAA J.*, Vol. 35, No. 5, 1997.

[10] Crook, A. and Wood, N. J., "Measurements and Visualizations of Synthetic Jets," AIAA 2001-0145, 2001.

[11] Rizzetta, D. P., Visbal, M. R., and Stanek, M. J., "Numerical Investigation of Synthetic-Jet Flow Fields," *AIAA J.*, Vol. 37, No. 8, pp. 919-927, 1999.

[12] Kral, L. D., Donovan, J. F., Cain, A. B., and Cary, A. W., "Numerical Simulation of Synthetic Jet Actuators," AIAA 97-1824, 1997.

[13] Mittal, R. and Rampunggoon, P., "On the Virtual Aeroshaping Effect of Synthetic Jets," *Phys. Fluids*, Vol. 14, No.4, pp. 1533-1536, 2002.

[14] Ravi, B. R., Mittal, R., and Najjar, F. M., "Study of 3-Dimensional Synthetic Jet Flowfields Using Direct Numerical Simulation," AIAA Paper 2004-0091, 2004.

[15] Cui, J., Agarwal, R. K., and Cary, A. W., "Numerical simulation of the Interaction of a Synthetic Jet with a Turbulent Boundary Layer," AIAA 2003-3458, 2003.

[16] Gordon, M. and Soria, J., "PIV Measurement of a Zero-Net Mass Flux Jet in Crossflow," *Exp. in Fluids*, Vol. 33, pp. 863-872, 2002.

[17] Panton, R. L., Incompressible Flow, John Wiley & Sons, Chapter 11, 1984.

[18] McCormick, D. C., "Boundary Layer Separation Control with Directed Synthetic Jets," AIAA Paper 2000-0519, Jan. 2000.

[19] Gallas, Q., Holman, R., Nishida, T., Carroll, B., Sheplak, M., and Cattafesta, L., "Lumped Element Modeling of Piezoelectric-Driven Synthetic Jet Actuators," *AIAA J.*, Vol. 41, No. 2, pp. 240-247, 2003.

[20] Ingard, U., and Labate, S., ''Acoustic Circulation Effects and the Nonlinear Impedance of Orifices,'' *J. Acoust. Soc. Am.*, Vol. 22, pp. 211–218, 1950.

[21] Seifert, A. and Pack, L. G., "Oscillatory Control of Separation at High Reynolds Numbers", *AIAA J.*, Vol. 37, No. 9, pp. 1062-1071, 1999.

[22] Smith, B. L., and Swift, G. W., "Power Dissipation and Time-Averaged Pressure in Oscillating Flow Through a Sudden Area Change," *J. Acoust. Soc. Am.*, Vol. 113, No. 5, May 2003.

[23] Schultz, T., Cattafesta, L., Nishida, T., and Sheplak, M., "Uncertainty Analysis of the Two-Microphone Method for Acoustic Impedance Testing," submitted to *Journal of Sound and Vibration.*

[24] Zang, Y., Street, R. L., and Koseff, J. R., "A non-staggered Grid, Fractional Step Method for Time-Dependent Incompressible Navier-Stokes Equations in Curvilinear Coordinates," *J. Comput. Phys.* 114, 18, 1994.

[25] Ye, T., Mittal, R., Udaykumar, H. S. and Shyy, W., "An Accurate Cartesian Grid Method for Viscous Incompressible Flows with Complex Immersed Boundaries," *J. Comp. Phys.* Vol. 156, pp. 209-240, 1999.

[26] Ghias, R., Mittal, R., and Lund, T., S., "A Non-Body Conformal Grid Method for Simulation of Compressible Flows with Complex Immersed Boundaries," AIAA Paper 2004-0080, Jan. 2004.

[27] Najjar, F. M., and Mittal, R., "Simulations of Complex Flows and Fluid-Structure Interaction Problems on Fixed Cartesian Grids," FEDSM 2003-45577, *Proceedings of FEDSM'03*, 4th ASME-JSME Joint Fluids Engineering Conference, July 2003.

[28] Utturkar, Y., "Numerical Investigation of Synthetic Jet Flow Fields," MS Thesis, Department of Mechanical Engineering , University of Florida, 2002.

[29] Utturkar, Y., Holman, R., Mittal, R., Carroll, B., Sheplak, M. and Cattafesta, L., "A Jet Formation Criterion for Synthetic Jet Actuators," AIAA Paper 2003-0636, Jan. 2003.

[30] White, F. M., Viscous Fluid Flow, McGraw Hill, pp.135-136, 1991.